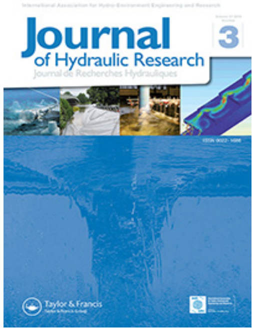

Journal of Hydraulic Research

ISSN: 0022-1686 (Print) 1814-2079 (Online) Journal homepage: https://www.tandfonline.com/loi/tjhr20

# Mesoscopic-based finite volume solutions for waterhammer flows

Sara Mesgari Sohani & Mohamed Salah Ghidaoui

**To cite this article:** Sara Mesgari Sohani & Mohamed Salah Ghidaoui (2019) Mesoscopic-based finite volume solutions for waterhammer flows, Journal of Hydraulic Research, 57:3, 337-352, DOI: 10.1080/00221686.2018.1522376

**To link to this article:** https://doi.org/10.1080/00221686.2018.1522376

*Journal of Hydraulic Research* Vol. 57, No. 3 (2019), pp. 337–352
https://doi.org/10.1080/00221686.2018.1522376

Research paper

# Mesoscopic-based finite volume solutions for waterhammer flows

SARA MESGARI SOHANI, Graduate MPhil Student, *Civil Department, Hong Kong University of Science and Technology, Hong Kong, PR China*
*Email:* *cemesgari@connect.ust.hk* *(author for correspondence)*

MOHAMED SALAH GHIDAOUI (IAHR Member), Chinese Estates Professor of Engineering and Chair Professor,
*Civil Department, Hong Kong University of Science and Technology, Hong Kong, PR China*
*Email:* *ghidaoui@ust.hk*

## ABSTRACT

It is becoming evident that high resolution finite volume (FV) numerical schemes for multi-dimensional waterhammer problems are needed for the development of an accurate transient-based condition assessment of pipelines. As a prerequisite, FV methods for one-dimensional waterhammer flows need to be developed. Such models can then be applied to multi-dimensional problems via directional splitting. In this paper, two FV schemes (one uses Bhatnagar–Gross–Krook Boltzmann (BGK) and the other uses kinetic flux vector splitting (KFVS) in the flux approximation) for one-dimensional waterhammer problems are formulated and applied. It is found that the KFVS and BGK schemes correctly capture discontinuity fronts in a classical reservoir-pipe-valve system. An oscillation-free collision time formulation has been proposed, tested and found to be robust. The stability of the proposed schemes is guaranteed when $C_r < 0.5$. Comparison between the BGK, KFVS, fixed-grid MOC, and first and second order Godunov schemes reveals that the second-order Godunov performs best, followed closely by the BGK scheme. However, the BGK should not be quickly dismissed since it is known that its real power becomes evident when dealing with complex physics, multi-scale and multi-dimensional problems.

*Keywords:* Boltzmann method; finite volume; high frequency wave; one-dimensional method; waterhammer

## 1 Introduction

The method of characteristics (MOC) is the most popular technique for solving water hammer problems. In fact, out of 14 commercially available water hammer software packages found in the World Wide Web, 11 are based on MOC (Ghidaoui, Zhao, McInnis, & Axworthy, 2005). The attributes of MOC include (i) ability to handle complex boundary conditions, (ii) efficiency due to its explicit nature, (iii) ease of coding, and (iv) inherent hyperbolic nature. The drawbacks of MOC include (i) difficulty in handling multi-dimensional waves, (ii) difficulty in handling flows with variable wave speeds, and (iii) discretization problems that arise when modelling multi-pipe systems (Ghidaoui & Karney, 1994). These drawbacks are largely inconsequential for classical water hammer applications such as design and analysis of pipe systems and their pressure and flow controls.

Recently, water hammer (transient) waves have been noted for their potential to detect defects such as leakages and partial blockages in pipes. As a result, the field of transient-based defect detection is an active area of research around the world (Duan, Lee, & Ghidaoui, 2014; Lee, Duan, Tuck, & Ghidaoui, 2014; Meniconi et al., 2013). The spatial resolution of the probing water hammer waves is an essential property underlying transient based defect detection. Physically, the spatial resolution of the transient-based defect detection method is of the order of $a/\omega$, where $a$ is the wave speed and $\omega$ is the frequency of the probing wave. Therefore, an increase in the wave frequency is accompanied by an increase in spatial resolution. Consider a typical value of $a = 1000\ \mathrm{m\,s^{-1}}$. The spatial resolution with $\omega = 10\,\mathrm{Hz}$ and $\omega = 10\,\mathrm{kHz}$ are 100 m and 0.1 m, respectively. Therefore, higher frequencies offer better localization of defects in pipe systems. In fact, the second author of this paper leads a large research program, Smart Urban Water Supply Systems (Smart UWSS), with one of its objectives being the development of high frequency methodology for pipe condition assessment (see http://smartuws.ust.hk/). The high frequency waves (as high as 100 kHz) have been tested numerically (Duan et al., 2017; Louati & Ghidaoui, 2017; Zhao, Ghidaoui, Louati, & Duan, 2018) as well as in the lab and field (Lee, Tuck, Davidson, & May, 2017; Li, Jing, & Murch, 2017)

The classical one-dimensional water hammer wave theory in which pressure waves are assumed to travel along pipes is

---

Received 25 November 2015; accepted 7 September 2018/Open for discussion until 31 December 2019.

ISSN 0022-1686 print/ISSN 1814-2079 online
http://www.tandfonline.com

valid for frequencies of the order of $L/a$, where $L$ is the length of the pipe under investigation. For example, for $L = 1000$ m and $a = 1000$ m s$^{-1}$, the classical one-dimensional water hammer wave theory is valid for frequencies of the order of 1 Hz. This is far below the desired frequencies of tens of kHz. In fact, for frequencies of the order of $D/a$, three-dimensional waves arise, where $D$ is the diameter of the pipe under investigation. Such three-dimensional waves not only go back and forth along pipes but also travel radially between the centre and the wall of pipes. For example, for $D = 100$ mm and $a = 1000$ m s$^{-1}$, three-dimensional water hammer waves arise if the probing signal has frequency of the order of 10 kHz. Therefore, three-dimensional water hammer wave theory is essential for the development of high spatial resolution transient based defect detection techniques.

MOC is impractical for three-dimensional water hammer wave theory. On the other hand, high resolution finite volume (FV) methods are well suited for three-dimensional wave problems. The modelling of fluxes at cell interfaces is either accomplished by macroscopic (Toro, 1999) or mesoscopic methods (Xu, 1998). Macroscopic methods are based on the Riemann solution while mesoscopic methods are based on the Boltzmann equation. The approach is often to develop such methods for one-dimensional problems. Directional splitting is, then, used to turn a multi-dimensional problem into a set of one-dimensional problems where the methods developed for one-dimensional problems apply along each of the flow direction being considered. The fact that water hammer problems are low Mach number flows means that the nonlinear advective terms are negligible and that directional (operator) splitting is a good approach for multi-dimensional water hammer waves. That is, the development of one-dimensional FV methods for water hammer flows is the prerequisite for the progress of high frequency wave theory in pipes. The Riemann based FV method has been applied to one-dimensional water hammer problems (Guinot, 2000; Hwang & Chung, 2002; Zhao & Ghidaoui, 2004) and two-dimensional water hammer problems (Louati & Ghidaoui, 2016). However, to the authors' knowledge, Boltzmann-based FV methods have not been applied to water hammer problems. Therefore, the objective of this paper is to develop a Boltzmann-based FV method for water hammer and test it against MOC, and Riemann-based FV methods.

Mesoscopic schemes can be broadly classified into (i) BGK models, which are FV schemes that use the Bhatnagar–Gross–Krook Boltzmann equation to model the fluxes; and (ii) LB schemes, which solve the lattice Boltzmann equation. In the LB scheme, particle velocities are discrete, but the BGK scheme velocity-distribution functions are continuous. Yongguang, Shihua, and Jianzhi (1998) and Cheng, Zhang, and Chen (1998) successfully utilized the LB scheme to simulate classical water hammer problems. Of concern to this paper is the BGK scheme. The BGK scheme is known to possess excellent shock capturing ability and high accuracy for viscous flow simulations (Xu & He, 2003). The collision-less Boltzmann scheme (e.g. the kinetic flux vector splitting (KFVS) scheme) was also formulated using a continuous velocity-distribution function while disregarding the collision term. Although the KFVS scheme lacks particle collisions in the evolution stage, it still gives reasonable numerical solutions (Xu, 1998). The BGK and KFVS schemes have been applied to a number of complex fluid problems such as shock waves in compressible flows (Xu, Kim, Martinelli, & Jameson, 1996), multicomponent and multiphase flows (Xu, 1997), low Mach number flows (Xu & He, 2003), heat transfer and reaction diffusion flows (Xu, 1999), shallow water flows and mass transportation phenomena (Ghidaoui, Deng, Gray, & Xu, 2001; Ghidaoui & Liang, 2008; Li, 2001; Liang, Ghidaoui, Deng, & Gray, 2007; Zhang, Ghidaoui, Gray, & Li, 2003), hypersonic viscous flows (Xu, Mao, & Tang, 2005), and micro-scale fluid flows (Liu, Xu, Zhu, & Ye, 2012). To our knowledge, no water hammer model based on the BGK or KFVS scheme has been developed so far. Such models are developed and applied in this paper. The authors of this paper also applied the BGK and KFVS schemes on moderately complex pipe systems. The pipe systems include different boundary conditions such as junctions where pipes' cross-sectional area change, leakage where fluid leaves out pipes, and joints of two pipes in which waves travel with different speeds. Using the BGK and KFVS schemes, the authors proposed a unified finite volume scheme in which boundary conditions are embedded. They successfully captured the wave interaction with boundary conditions. To make the current paper short, details of the unified finite volume scheme are presented in another paper named "Formulation of consistent finite volume schemes for hydraulic transients" (Mesgari Sohani & Ghidaoui, 2018).

## 2 Mesoscopic models for water hammer problems

The fundamental equation in the kinetic approach was established by Boltzmann in 1872 (Cercignani, 1988; Ghidaoui, 2008). The Boltzmann equation originally models the dynamics of rarefied gases via a time-dependent density of particles (namely, $f(\boldsymbol{X}, t, \boldsymbol{C})$) in a six-dimensional phase space (i.e. $x, y, z, c_x, c_y, c_z$, where subscripts represent spatial directions) (Villani, 2008; Vincenti & Kruger, 1965). The Boltzmann equation with external force boundaries is:

$$\frac{\partial f}{\partial t} + \underbrace{\boldsymbol{C} \cdot \nabla f}_{\text{Advection}} + \underbrace{\boldsymbol{F}' \cdot \frac{\partial f}{\partial \boldsymbol{C}}}_{\text{Acceleration}} = \underbrace{Q'(f)}_{\text{Collision}} \tag{1}$$

where $\boldsymbol{C} = [c_x, c_y, c_z]^{\mathrm{T}}$ are the particles velocities; $\boldsymbol{F}' = [F'_x, F'_y, F'_z]^{\mathrm{T}}$ are the external forces; $\boldsymbol{C} \cdot \nabla$ is the advection operator; $\boldsymbol{F}' \cdot (\partial/\partial \boldsymbol{C})$ is the acceleration operator; and $Q'$ is the collision operator. Theoretically, the range of particle velocities ($c_x$, $c_y$, and $c_z$) is the whole real line. Boltzmann also introduced

H-theorem function that states:

$$S(f) = -H(f) = -\iiint f\ \ln(f)\,\mathrm{d}c_x\,\mathrm{d}c_y\,\mathrm{d}c_z \tag{2}$$

where $S$ is the entropy. Boltzmann's H-theorem is of basic importance because it shows that the Boltzmann equation ensures irreversibility (Xu, 1998). In addition, it is used to achieve an equilibrium velocity-distribution function. As $S$ increases and achieves its maximum, a non-equilibrium velocity-distribution function ($f$) approaches an equilibrium velocity-distribution function denoted by $g$.

The collision operator term in Eq. (1) prevents us from obtaining an exact solution of the Boltzmann equation due to the operator's complexity. Therefore, approximate forms of this operator have been proposed over the last century (Cercignani, 1988). Among these approximate methods, the model proposed by Bhatnagar–Gross–Krook in 1954 ( the BGK model) is the most popular in fluid applications because of its simplicity and accuracy. The one-dimensional BGK Boltzmann equation without external forces, then, is:

$$\frac{\partial f}{\partial t} + c_x\frac{\partial f}{\partial x} = \frac{g-f}{\tau} \tag{3}$$

where $\tau$ is the average time interval between successive particle collisions. Moreover, the fundamental laws of classical physics dictate that the mass, momentum, and energy of the particles are collision invariant (Vincenti & Kruger, 1965). Therefore:

$$\int_{-\infty}^{+\infty}\begin{bmatrix}1\\ c_x\\ c_x^2\end{bmatrix}\frac{g-f}{\tau}\mathrm{d}c_x = \begin{bmatrix}0\\0\\0\end{bmatrix} \tag{4}$$

The above relation is often called the compatibility condition. The collision term in the BGK model causes the equilibrium velocity-distribution function ($g$) to deviate from the non-equilibrium velocity-distribution function ($f$). This makes the BGK model capable of capturing both equilibrium and non-equilibrium gas flow accurately and robustly (Vincenti & Kruger, 1965; Xu, 1998). A bridge between the BGK Boltzmann equation on the one side and Navier–Stokes or Euler equations on the other side is established using the Chapman–Enskog expansion solution (Kogan, 1967). Throughout the established connection, the collision term $\tau$ needs to be a function of the local macroscopic flow variables as follows (Xu, 1998):

$$\tau = \frac{\mu}{P} \tag{5}$$

where $\mu$ is the dynamic viscosity; $P$ is the fluid pressure.

Any mesoscopic-based scheme is initially constructed from the BGK Boltzmann equation and then specified to describe a certain type of fluid applications. In the next section, the one-dimensional BGK Boltzmann equation (Eq. (3)) is specified for water hammer problems.

### 2.1 *Specification of mesoscopic-based equations for water hammer applications*

Boltzmann-based models were originally established for gas flow in which pressure is coupled with flow density and temperature through the gas flow state equation. (Xu, 1998). In water hammer, however, temperature is decoupled from pressure due to relatively large specific heat of water. Thus, the state equation fitted for water hammer applications is $\mathrm{d}P/\mathrm{d}\rho = a^2$, where $a$ is the transient wave speed (Chaudhry, 1979). It is worth mentioning that in the classical water hammer model, wave speed includes both water and pipe wall effects in the formulation (Chaudhry, 1979), whereas in the mesoscopic-based approaches, wave speed only bears the elasticity of fluid and excludes the wall effects (i.e. the rigid pipe assumption). In the other words, the mesoscopic-based models solve fluid in pipes and exclude any interaction between fluid and pipe walls. To include the wall elasticity in the current formulation, however, the mesoscopic-based models are able to adopt the wall elasticity effect as external forces in formulation. Such a practice is outside the scope of the current study and is left for future studies.

Using the Boltzmann H-theorem (see Appendix), the specification of velocity-distribution function for one-dimensional water hammer problems at the equilibrium state, then, gives:

$$g = \rho\sqrt{\frac{\lambda}{\pi}}e^{-\lambda(c_x-u)^2} \tag{6}$$

where $\lambda = 1/(2a^2)$ is constant as the wave propagation speed ($a$) is constant; $\rho$ is the macroscopic density; and $u$ is the macroscopic flow velocity in $x$-direction which is equal to the macroscopic average flow velocity in $x$-direction ($U$) in the current one-dimensional water hammer model. The statistical moments of $g$ (i.e. the zero, first, second moments of $g$) provide the macroscopic flow variables:

$$\begin{bmatrix}\rho\\ \rho u\\ \rho\left(u^2+\dfrac{P}{\rho}\right)\end{bmatrix} = \int_{-\infty}^{+\infty}\begin{bmatrix}1\\ c_x\\ c_x^2\end{bmatrix} g\,\mathrm{d}c_x \tag{7}$$

The link between one-dimensional BGK equation and the classical one-dimensional water hammer equation can be established using two steps. In the first step, the compressible one-dimensional Navier–Stokes equations can be derived from the one-dimensional BGK equation using the Chapman–Enskog expansion (Kogan, 1967). In the second step, the one-dimensional water hammer equations are obtained by combining the state equation $\mathrm{d}P/\mathrm{d}\rho = a^2$ with the compressible one-dimensional Navier–Stokes equation (Ghidaoui et al., 2005). The fact that one-dimensional water hammer equations are obtainable from the one-dimensional BGK equation is exploited here to formulate FV fluxes on the basis of solving the BGK equation. In coming sections, first, a finite volume mesoscopic-based scheme is built then the fluxes are determined using the mesoscopic approaches.

## 2.2 *Discrete mesoscopic-based FV*

The mesoscopic-based schemes are established in a finite volume framework in which an integral form of the BGK equation (Eq. (3)) is applied on flow inside a pipe (i.e. a space domain). Due to restriction of the space domain in its boundaries, the formulation of BGK scheme is needed to be customized inside the intact pipe and its two ends, separately.

### *An intact pipe*

Figure 1 shows a one-dimensional discrete space domain, a pipe of length $L$. The space domain is equally discretized to $N_x$ cells of width $\Delta x$ (i.e. $\Delta x = L/N_x$). Cell ($i$), $i \in [1, N_x]$, is confined to the interface $x = x_{i-1/2}$ and the interface $x = x_{i+1/2}$. The flow variables ($\rho$ and $\rho u$) are assumed to be the piecewise constant, namely $\overline{\boldsymbol{W}}_i^n = [\overline{\rho}_i^n, \overline{\rho u}_i^n]^{\mathrm{T}}$ inside cell ($i$) at time step $n$. The over-line notation indicates the cell-averaged flow variables. $\boldsymbol{F}_{i-1/2}$ and $\boldsymbol{F}_{i+1/2}$ are the numerical fluxes across the interface $x = x_{i-1/2}$ and the interface $x = x_{i+1/2}$, respectively.

Applying integral form of the BGK equation (Eq. (3)) on cell ($i$) shown in Fig. 1 from time $t^n$ to time $t^{n+1}$, then, gives:

$$\int_{x_{i-1/2}}^{x_{i+1/2}} (f^{n+1} - f^{n})\,\mathrm{d}x = \int_{t^n}^{t^{n+1}} c_x (f_{x_{i-1/2}})\,\mathrm{d}t - \int_{t^n}^{t^{n+1}} c_x (f_{x_{i+1/2}})\,\mathrm{d}t + \int_{t^n}^{t^{n+1}} \int_{x_{i-1/2}}^{x_{i+1/2}} \frac{g - f}{\tau}\,\mathrm{d}x\,\mathrm{d}t \tag{8}$$

Taking the zero and first moments of Eq. (8) gives how flow variables inside cell ($i$) evolve from time $t^n$ to time $t^{n+1}$ as follows:

$$\overline{\boldsymbol{W}}_i^{n+1} = \overline{\boldsymbol{W}}_i^{n} + \frac{1}{\Delta x}(\boldsymbol{F}_{i-1/2} - \boldsymbol{F}_{i+1/2}) \tag{9}$$

where

$$\Delta x = x_{i+1/2} - x_{i-1/2}, \quad \Delta t = t^{n+1} - t^n, \quad \overline{\boldsymbol{W}} = \begin{bmatrix} \overline{\rho} \\ \overline{\rho u} \end{bmatrix} \tag{10}$$

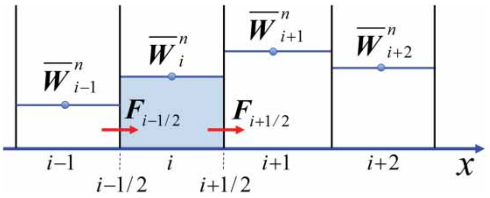

Figure 1 Discrete space domain

$$\boldsymbol{F}_{i-1/2} = \int_0^{\Delta t} \int_{-\infty}^{+\infty} c_x f_{i-1/2} \begin{bmatrix} 1 \\ c_x \end{bmatrix} \mathrm{d}c_x\,\mathrm{d}t,$$

$$\boldsymbol{F}_{i+1/2} = \int_0^{\Delta t} \int_{-\infty}^{+\infty} c_x f_{i+1/2} \begin{bmatrix} 1 \\ c_x \end{bmatrix} \mathrm{d}c_x\,\mathrm{d}t \tag{11}$$

$\boldsymbol{F}_{i-1/2}$ and $\boldsymbol{F}_{i+1/2}$ are mesoscopic-based and time-dependent fluxes at the interface $x = x_{i-1/2}$ and the interface $x = x_{i+1/2}$, respectively. The last term in Eq. (3) disappears due to the compatibility conditions (i.e. Eq. (4)), so the collision term has no direct influence on the update of conservative variables inside each cell.

The FV Boltzmann-based model (Eq. (9)) solves the density and mass flux ($\rho$ and $\rho u$), whereas the classical water hammer solution solves the pressure head and flow rate ($H$ and $Q$). In order to compare the classical water hammer solution to the proposed Boltzmann-based scheme, a map is required to relate $\rho$ and $\rho u$ to $H$ and $Q$, respectively. The state equation ($\mathrm{d}P/\mathrm{d}\rho = a^2$) can relate the density to the pressure head. Integration of the state equation leads to:

$$P = a^2 \rho \tag{12}$$

where $P = P_1 - P_0$ is the pressure fluctuation due to any transient, $\rho = \rho_1 - \rho_0$ is the density fluctuation due to any transient. $P_0$ and $\rho_0$ are the pressure and density before any disturbance. Eq. (12) in the form of pressure head becomes:

$$H = \frac{\rho a^2}{9.81 \rho_0} \tag{13}$$

Flow rate also can be obtained from the below relationship:

$$Q = \frac{\rho u A}{\rho_0} \tag{14}$$

where $A$ is the pipe cross-sectional area. Using the map (Eqs (13) and (14)), the numerical results associated with the KFVS and BGK schemes can be represented in the form of pressure head and flow rate, notwithstanding that the original Boltzmann-based equation solves the density and mass flux.

### *Valve and reservoir*

The valve is locally placed at the interface between cell ($i = N_x$) and fictitious cell ($i = N_x + 1$) denoted by the subscript $_{vf}$. The reservoir is located at the interface between fictitious cell ($i = 0$) denoted by the subscript $_{rf}$ and cell ($i = 1$). A water hammer wave is initiated by an instantaneous closure of the valve. At the closed valve, the impedance is infinite. As a result:

$$\rho_{vf} = \rho_{N_x} \quad \text{and} \quad (\rho U)_{vf} = -(\rho U)_{N_x} \tag{15}$$

where $U$ is the macroscopic average velocity. The reservoir maintains a constant pressure at the interface between fictitious cell ($i = 0$) and cell ($i = 1$). Therefore, the pressure wave fluctuation and the impedance at the reservoir are zero, which implies:

$$\rho_{rf} - \rho_0 = -(\rho_1 - \rho_0) \quad \text{and} \quad (\rho U)_{rf} = (\rho U)_1 \tag{16}$$

where the fact that $P = a^2\rho$ (Eq. (12)) has been used; and $\rho_0$ is the fluid density before any disturbance.

### 2.3 *High-order flux approximation using reconstruction*

The time-dependent fluxes in Eq. (11) are calculated at cell interfaces where the flow variables and the velocity-distribution function may experience a discontinuity. To achieve a high-resolution scheme, a piecewise linear function within each cell as shown in Fig. 2 is applied.

Using a 2nd-order Taylor expansion around cell-averaged values, the flow variables within cell ($i$) at time step $n$ become:

$$\boldsymbol{W}_i^n(x) = \overline{\boldsymbol{W}}_i^n + (x - x_i)\left(\frac{\partial \boldsymbol{W}}{\partial x}\right)_i^n \quad \text{where } x \in [x_{i-1/2}, x_{i+1/2}] \tag{17}$$

where $\overline{\boldsymbol{W}}$ is the cell-averaged flow variables; and $(\partial \boldsymbol{W}/\partial x)_i^n$ is the gradient of flow variables within cell ($i$). The 2nd-order scheme offers less numerical dissipation, but may produce non-physical oscillations near large gradients (Hirsch, 2007). One way to suppress the numerical oscillations is to add artificial dissipation terms to the scheme. However it is difficult to find an appropriate artificial dissipation term to maintain monotonicity but avoid unnecessary smearing (Ghidaoui et al., 2001). The other alternative to produce a monotone solution is applying limiters (i.e. slope limiters) to the reconstructed fluid states at each time step. The basic notion behind limiters is to control the generation of over- and under-shoots by preventing slopes to exceed certain limits. In this way, the oscillations whose origins are in numerical approximations are cured at the generation stage by keeping the slopes in an appropriate bound within each cell (Hirsch, 2007).

To guarantee an oscillation-free 2nd-order scheme, the Van Leer limiter (Hirsch, 2007; Van Leer, 1997) is used to approximate a proper gradient for flow variables as follows:

$$\left(\frac{\partial \boldsymbol{W}}{\partial x}\right)_i^n = \begin{bmatrix} \frac{\partial \rho}{\partial x} \\ \frac{\partial (\rho u)}{\partial x} \end{bmatrix}_i^n = \frac{1}{2\Delta x}\begin{bmatrix} \mathrm{sign}(\rho_i - \rho_{i-1}, \rho_{i+1} - \rho_i)\dfrac{|\rho_i - \rho_{i-1}||\rho_{i+1} - \rho_i|}{|\rho_i - \rho_{i-1}| + |\rho_{i+1} - \rho_i|} \\ \mathrm{sign}((\rho u)_i - (\rho u)_{i-1}, (\rho u)_{i+1} - (\rho u)_i)\dfrac{|(\rho u)_i - (\rho u)_{i-1}||(\rho u)_{i+1} - (\rho u)_i|}{|(\rho u)_i - (\rho u)_{i-1}| + |(\rho u)_{i+1} - (\rho u)_i|} \end{bmatrix}^n \tag{18}$$

The Van Leer limiter function is a sort of second order TVD. This means that they are designed to pass through a certain region of the solution, known as the TVD region, to guarantee stability. These limiters do not ensure the satisfaction of the entropy condition (Hirsch, 2007). However, the entropy condition is intrinsically held in Boltzmann-based equations (Xu, 1998). Lui and Xu (2001) also proved that entropy condition for the KFVS scheme and concluded that the KFVS scheme is robust for CFD applications.

Knowing the slopes within each cell, the flow variables at the left and right sides of the interface $x = x_{i-1/2}$, denoted by a negative sign for the left side and a positive sign for the right side, are obtained from the linear extrapolation of cell-averaged values (see the magnified region in Fig. 2):

$$\boldsymbol{W}_{i-1/2^-}^n = \overline{\boldsymbol{W}}_{i-1}^n + 0.5\Delta x\left(\frac{\partial \boldsymbol{W}}{\partial x}\right)_{i-1}^n \quad \text{and}$$
$$\boldsymbol{W}_{i-1/2^+}^n = \overline{\boldsymbol{W}}_i^n - 0.5\Delta x\left(\frac{\partial \boldsymbol{W}}{\partial x}\right)_i^n \tag{19}$$

In the next sections, high-order fluxes at the interface $x = x_{i-1/2}$ can be calculated from $\boldsymbol{W}_{i-1/2^-}^n$ and $\boldsymbol{W}_{i-1/2^+}^n$ instead of $\overline{\boldsymbol{W}}_{i-1}^n$ and $\overline{\boldsymbol{W}}_i^n$ using the KFVS and BGK approaches, respectively.

#### *Flux approximation using the KFVS scheme*

To determine unique time-dependent mass and momentum fluxes at the interface $x = x_{i-1/2}$ (i.e. $\boldsymbol{F}_{i-1/2}$), a unique velocity-distribution function ($f_{i-1/2}$) is required to obtain at the interface $x = x_{i-1/2}$. However, it is unlikely to achieve such a velocity-distribution function in typical water hammer problems since a discontinuity in flow fields is physically imposed. Nevertheless, the KFVS scheme offers that a unique velocity-distribution function can be approximated if the velocity-distribution function can be split in the term of particle speeds (Li, 2001; Xu, 1998; Zhang et al., 2003). In the KFVS approach, particles move freely with positive and negative speeds across interfaces. The freely movement is implied from the analytical solution of the collision-less Boltzmann equation as follows:

$$f(x) = f_0(x - c_x t) \tag{20}$$

where $f_0$ is the velocity-distribution function at the initial condition. The splitting notion of the KFVS scheme, however,

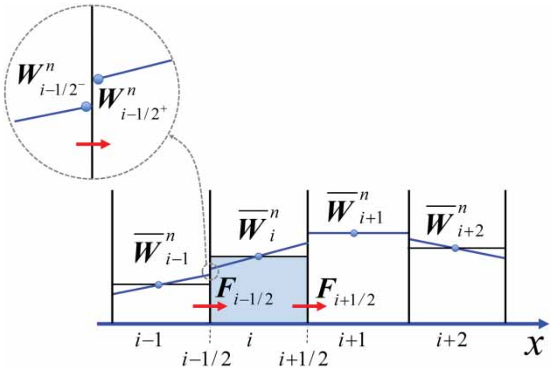

Figure 2 Data reconstruction under the slope limiter

proposes that particles with positive speed travel forward but particles whose speed are negative travel backward, so a 2nd-order approximation of the velocity-distribution function at time step $n$ around the interface $x = x_{i-1/2}$ gives (Li, 2001; Xu, 1998; Zhang et al., 2003):

$$f\,(x_{i-1/2}, t, c_x) = \begin{cases} g^n_{i-1/2^-} + \left(\frac{\partial g}{\partial x}\right)^n_{i-1/2^-} (x - x_{i-1/2}) & x \le x_{i-1/2} \text{ and } c_x \ge 0 \\ g^n_{i-1/2^+} + \left(\frac{\partial g}{\partial x}\right)^n_{i-1/2^+} (x - x_{i-1/2}) & x > x_{i-1/2} \text{ and } c_x < 0 \end{cases} \tag{21}$$

where

$$x = x_{i-1/2} - c_x t, \tag{22}$$

$$g^n_{i-1/2^-} = \left[\rho\sqrt{\frac{\lambda}{\pi}}e^{-\lambda(c_x-u)^2}\right]^n_{i-1/2^-},$$
$$g^n_{i-1/2^+} = \left[\rho\sqrt{\frac{\lambda}{\pi}}e^{-\lambda(c_x-u)^2}\right]^n_{i-1/2^+} \tag{23}$$

$$\left(\frac{\partial g}{\partial x}\right)^n_{i-1/2^-} = g^n_{i-1/2^-}\left[\left(\frac{1}{\rho} + \frac{2\lambda u^2}{\rho}\right)\frac{\partial \rho}{\partial x} - \frac{2\lambda u}{\rho}\frac{\partial(\rho u)}{\partial x} + c_x\left(-\frac{2\lambda}{\rho}\frac{\partial(\rho u)}{\partial x} + \frac{2\lambda u}{\rho}\frac{\partial \rho}{\partial x}\right)\right]^n_{i-1/2^-} \tag{24}$$

$$\left(\frac{\partial g}{\partial x}\right)^n_{i-1/2^+} = g^n_{i-1/2^+}\left[\left(\frac{1}{\rho} + \frac{2\lambda u^2}{\rho}\right)\frac{\partial \rho}{\partial x} - \frac{2\lambda u}{\rho}\frac{\partial(\rho u)}{\partial x} + c_x\left(-\frac{2\lambda}{\rho}\frac{\partial(\rho u)}{\partial x} + \frac{2\lambda u}{\rho}\frac{\partial \rho}{\partial x}\right)\right]^n_{i-1/2^+} \tag{25}$$

The variables in the left and right sides of the interface $x = x_{1-1/2}$ are denoted by $-$ and $+$, respectively. The slopes of the macroscopic flow variables ($\partial\rho/\partial x$ and $\partial(\rho u)/\partial x$) in the left and right side of the interface $x = x_{i-1/2}$ have already been determined from the data reconstruction step (Eq. (18)). Substituting Eq. (21) into Eq. (11) gives the 2nd-order approximation of time-dependent mass and momentum fluxes at the interface $x = x_{i-1/2}$:

$$\begin{aligned} \boldsymbol{F}_{i-1/2} &= \int_0^{\Delta t}\int_{-\infty}^{+\infty} c_x f_{i-1/2}\begin{bmatrix}1\\ c_x\end{bmatrix} \mathrm{d}c_x \mathrm{d}t \\ &= \int_0^{\Delta t}\int_0^{+\infty} c_x\left(g^n_{i-1/2^-} - \left(\frac{\partial g}{\partial x}\right)^n_{i-1/2^-} c_x t\right)\begin{bmatrix}1\\ c_x\end{bmatrix} \mathrm{d}c_x \mathrm{d}t \\ &+ \int_0^{\Delta t}\int_{-\infty}^{0} c_x\left(g^n_{i-1/2^+} - \left(\frac{\partial g}{\partial x}\right)^n_{i-1/2^+} c_x t\right)\begin{bmatrix}1\\ c_x\end{bmatrix} \mathrm{d}c_x \mathrm{d}t \end{aligned} \tag{26}$$

The zero and first moments of Eq. (26) in terms of positive and negative particle speeds (see Appendix) give:

$$\begin{aligned} \boldsymbol{F}_{i-1/2} &= \int_0^{\Delta t}\int_{-\infty}^{+\infty} c_x f_{i-1/2}\begin{bmatrix}1\\ c_x\end{bmatrix} \mathrm{d}c_x\, \mathrm{d}t \\ &= \Delta t\begin{bmatrix} \frac{\rho u}{2}\mathrm{erfc}(-\sqrt{\lambda}u) + \frac{\rho e^{-\lambda u^2}}{2\sqrt{\pi\lambda}} \\ \frac{\rho u^2+\rho/2\lambda}{2}\mathrm{erfc}(-\sqrt{\lambda}u) + \frac{\rho u e^{-\lambda u^2}}{2\sqrt{\pi\lambda}} \end{bmatrix}^n_{i-1/2^-} \\ &+ \Delta t\begin{bmatrix} \frac{\rho u}{2}\mathrm{erfc}(+\sqrt{\lambda}u) - \frac{\rho e^{-\lambda u^2}}{2\sqrt{\pi\lambda}} \\ \frac{\rho u^2+\rho/2\lambda}{2}\mathrm{erfc}(+\sqrt{\lambda}u) - \frac{\rho u e^{-\lambda u^2}}{2\sqrt{\pi\lambda}} \end{bmatrix}^n_{i-1/2^+} \\ &- \frac{\Delta t^2}{2}\begin{bmatrix} \langle c_x^2\rangle_{>0}\left(\left(\frac{1}{\rho} + \frac{2\lambda u^2}{\rho}\right)\frac{\partial\rho}{\partial x} - \frac{2\lambda u}{\rho}\frac{\partial(\rho u)}{\partial x}\right) \\ +\left\langle c_x^3\right\rangle_{>0}\left(\frac{-2\lambda}{\rho}\frac{\partial(\rho u)}{\partial x} + \frac{2\lambda u}{\rho}\frac{\partial\rho}{\partial x}\right) \\ \langle c_x^3\rangle_{>0}\left(\left(\frac{1}{\rho} + \frac{2\lambda u^2}{\rho}\right)\frac{\partial\rho}{\partial x} - \frac{2\lambda u}{\rho}\frac{\partial(\rho u)}{\partial x}\right) \\ +\left\langle c_x^4\right\rangle_{>0}\left(\frac{-2\lambda}{\rho}\frac{\partial(\rho u)}{\partial x} + \frac{2\lambda u}{\rho}\frac{\partial\rho}{\partial x}\right) \end{bmatrix}^n_{i-1/2^-} \\ &- \frac{\Delta t^2}{2}\begin{bmatrix} \langle c_x^2\rangle_{<0}\left(\left(\frac{1}{\rho} + \frac{2\lambda u^2}{\rho}\right)\frac{\partial\rho}{\partial x} - \frac{2\lambda u}{\rho}\frac{\partial(\rho u)}{\partial x}\right) \\ +\left\langle c_x^3\right\rangle_{<0}\left(\frac{-2\lambda}{\rho}\frac{\partial(\rho u)}{\partial x} + \frac{2\lambda u}{\rho}\frac{\partial\rho}{\partial x}\right) \\ \langle c_x^3\rangle_{<0}\left(\left(\frac{1}{\rho} + \frac{2\lambda u^2}{\rho}\right)\frac{\partial\rho}{\partial x} - \frac{2\lambda u}{\rho}\frac{\partial(\rho u)}{\partial x}\right) \\ +\left\langle c_x^4\right\rangle_{<0}\left(\frac{-2\lambda}{\rho}\frac{\partial(\rho u)}{\partial x} + \frac{2\lambda u}{\rho}\frac{\partial\rho}{\partial x}\right) \end{bmatrix}^n_{i-1/2^+} \end{aligned} \tag{27}$$

erfc is the complementary error function appearing in Eq. (27) because the velocity-distribution function is spilt in terms of positive and negative particle speeds. Equation (27) represents the 2nd-order approximation for time-dependent mass and momentum fluxes at the interface $x = x_{i-1/2}$. Excluding the last two terms in Eq. (27) reduces the accuracy of Eq. (27) to a 1st-order scheme. In an analogous way, time-dependent mass and momentum fluxes at any interface can be obtained.

### *Flux approximation using the BGK scheme*

In the BGK scheme, fluxes are calculated from the analytical solution of the BGK Boltzmann equation at the interface $x_{i-1/2}$ and at time $t$ as below (Cercignani, 1988; Ghidaoui, 2008):

$$f\,(x_{i-1/2}, t, c_x) = f_0(x_{i-1/2} - c_x t)e^{-t/\tau} + \frac{1}{\tau}\int_0^t g(x', t', c_x)e^{-(t-t')/\tau}\,\mathrm{d}t' \tag{28}$$

where $t'$ is a dummy variable; $x' = x_{i-1/2} - c_x(t - t')$ is the trajectory of a particle motion; $f_0(x_{i-1/2} - c_x t)$ is a not-equilibrium velocity-distribution function at the beginning of each time step; $g$ is an equilibrium velocity-distribution function both in space and in time around the point ($x = x_{i-1/2}, t = 0$); and $\tau$ is the particle collision time.

$\tau$ physically depends on the local macroscopic flow variables ($\tau = \mu/P$). However, due to the finite cell size and time step, the particle collision time used in the calculation also includes an artificial term to account for the fact that the smallest numerical shock thickness is the cell size instead of the physical shock thickness (Xu, 1998). The collision time is evaluated according to the form proposed by Xu (1998) at the interface $x = x_{i-1/2}$:

$$\tau_{i-1/2} = C_1 \frac{\mu_{i-1/2}}{p_{i-1/2}} + C_2 \frac{|p_{i-1} - p_i|}{|p_{i-1} + p_i|} \Delta t \tag{29}$$

where $C_1$ and $C_2$ are constants and are determined from numerical experimentations. Equation (29) may need to be modified for water hammer applications. The full discussion of the collision time modification is given in the next sections for a numerical test case.

At a non-equilibrium flow state, the numerical cell size is usually much larger than the thickness of a discontinuity, so physical quantities changing dramatically in space and flow properties ($\rho$ and $\rho u$) can experience large variations across a cell interface, for example across a wave front in water hammer flows. As a consequence, $\rho$ and $\rho u$ are discontinuous at cell interfaces as the left and right velocity-distribution functions could be two different Maxwellians. Therefore, the splitting of $f_0$ is required to capture this possible physical reality. The 2nd-order Taylor series expansions for $f_0$ around $x_{i-1/2^-}$ and $x_{i-1/2^+}$ are implemented as follows:

$$f_0 = \begin{cases} g_l + (\frac{\partial g}{\partial x})_l (x - x_{i-1/2}) & x \le x_{i-1/2} \quad c_x \ge 0 \\ g_r + (\frac{\partial g}{\partial x})_r (x - x_{i-1/2}) & x > x_{i-1/2} \quad c_x < 0 \end{cases} \tag{30}$$

where $x = x_{i-1/2} - c_x t$ is the particle location at time $t$; $g_l$ and $g_r$ are the local Maxwellian velocity-distribution functions located to the left and to the right of the interface $x = x_{i-1/2}$, respectively. $g_l$ and $g_r$ are evaluated from $\boldsymbol{W}^n_{i-1/2^-}$ and $\boldsymbol{W}^n_{i-1/2^+}$, respectively. $(\partial g/\partial x)_l$ and $(\partial g/\partial x)_r$ can be obtained from macroscopic flow located to the left and to the right of the interface $x = x_{i-1/2}$, respectively. As $\lambda = 1/2a^2$ is constant, the variation of $g$ with respect to $x$ gives:

$$\frac{\partial g}{\partial x} = (k_1 + k_2 c_x) g \tag{31}$$

where

$$\begin{aligned} k_1 &= \frac{1}{\rho}\frac{\partial \rho}{\partial x} - 2\lambda u \frac{\partial (\rho u)}{\partial x} + 2\lambda u^2 \frac{\partial \rho}{\partial x}, \\ k_2 &= -2\lambda \frac{\partial (\rho u)}{\partial x} + 2\lambda u \frac{\partial \rho}{\partial x} \end{aligned} \tag{32}$$

$k_1 + k_2 c_x$ in Eq. (31) alternatively is denoted by $k$ and so-called the corresponding slope of Maxwellian function ($g$). $k$ is determined from the corresponding gradients of macroscopic variables. Particularly, $(\partial g/\partial x)_l$ and $(\partial g/\partial x)_r$ in Eq. (30) (see the magnified macroscopic region in Fig. 3) are obtained from corresponding gradients of macroscopic variables in the data reconstruction step (Eq. (18)). Substituting Eq. (31) into Eq. (30) leads to:

$$f_0 = \begin{cases} g_l (1 + k_l (x - x_{i-1/2})) & x \le x_{i-1/2} \quad c_x \ge 0 \\ g_r (1 + k_r (x - x_{i-1/2})) & x > x_{i-1/2} \quad c_x < 0 \end{cases} \tag{33}$$

where $k_l = k_{l1} + k_{l2} c_x$ and $k_r = k_{r1} + k_{r2} c_x$. From Eq. (18), $k_{l1}$, $k_{l2}$, $k_{r1}$, and $k_{r2}$ can be calculated for the corresponding gradients of macroscopic variables in the initial reconstruction stage.

To evaluate the second term in the right hand side of Eq. (28), an approximate expression for the unique equilibrium velocity-distribution $g_0$ is required. $g$ for all $x$ and $t$ can be approximated from the 2nd-order Taylor expansion of $g_0$ around $(x = x_{i-1/2}, t)$ as follows:

$$g = \begin{cases} g_0 + (\frac{\partial g_0}{\partial x})_l (x - x_{i-1/2}) + \frac{\partial g_0}{\partial t} t & x \le x_{i-1/2} \quad c_x \ge 0 \\ g_0 + (\frac{\partial g_0}{\partial x})_r (x - x_{i-1/2}) + \frac{\partial g_0}{\partial t} t & x > x_{i-1/2} \quad c_x < 0 \end{cases} \tag{34}$$

where $g_0$ is a local Maxwellian velocity-distribution function located in the interface $x = x_{i-1/2}$ which gives $\boldsymbol{W}_0$ (i.e. a local macroscopic flow variables). $(\partial g_0/\partial x)_l$ and $(\partial g_0/\partial x)_r$ are the slope of macroscopic variables between the $\boldsymbol{W}_0$ and $\overline{\boldsymbol{W}}_{i-1}$ and $\overline{\boldsymbol{W}}_i$, respectively. $\partial g_0/\partial t$ is the temporal gradient and denoted by $K g_0$. For determining $g_0$, Xu (1998) suggested:

$$\int_{-\infty}^{+\infty} \begin{bmatrix} 1 \\ c_x \end{bmatrix} g_0 c_x \begin{bmatrix} 1 \\ c_x \end{bmatrix} \mathrm{d}c_x = \int_{-\infty}^{0} g_l c_x \begin{bmatrix} 1 \\ c_x \end{bmatrix} \mathrm{d}c_x + \int_{0}^{+\infty} g_r c_x \begin{bmatrix} 1 \\ c_x \end{bmatrix} \mathrm{d}c_x \tag{35}$$

where $g_l$ and $g_r$ are the local Maxwellian velocity-distribution functions located to the left and right sides of the interface $x = x_{i-1/2}$. The underling physical assumption in the above equation is that the left and right moving particles collapse at the interface $x = x_{i-1/2}$ to form an equilibrium state $g_0$ (see Fig. 3). Taking the zero and first moments of $g_0$ yields an unique macroscopic variable at the interface $x = x_{i-1/2}$ (i.e. $\boldsymbol{W}_0$):

$$\boldsymbol{W}_0 = \begin{bmatrix} \rho_0 \\ \rho_0 u_0 \end{bmatrix} = \int_{-\infty}^{+\infty} g_0 \begin{bmatrix} 1 \\ c_x \end{bmatrix} \mathrm{d}c_x \tag{36}$$

The reconstruction of the unique velocity-distribution function ($g_0$) re-establishes the corresponding slope as follows:

$$\left(\frac{\partial \boldsymbol{W}}{\partial x}\right)_{0l} = \begin{bmatrix} (\frac{\partial \rho}{\partial x})_{0l} \\ (\frac{\partial \rho u}{\partial x})_{0l} \end{bmatrix} = \begin{bmatrix} (\rho_0 - \overline{\rho}_{i-1})/(x_{i-1/2} - x_{i-1}) \\ (\rho_0 u_0 - \overline{\rho_{i-1} u_{i-1}})/(x_{i-1/2} - x_{i-1}) \end{bmatrix} \tag{37}$$

$$\left(\frac{\partial \boldsymbol{W}}{\partial x}\right)_{0r} = \begin{bmatrix} (\frac{\partial \rho}{\partial x})_{0r} \\ (\frac{\partial \rho u}{\partial x})_{0r} \end{bmatrix} = \begin{bmatrix} (\overline{\rho}_i - \rho_0)/(x_i - x_{i-1/2}) \\ (\overline{\rho_i u_i} - \rho_0 u_0)/(x_i - x_{i-1/2}) \end{bmatrix} \tag{38}$$

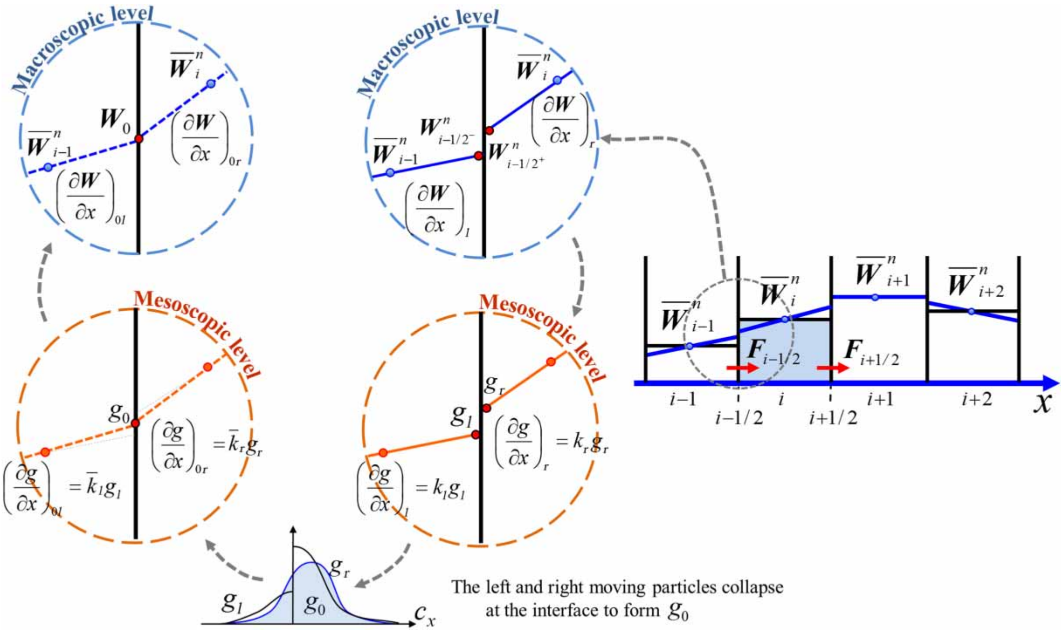

Figure 3 Calculation of $g_0$ and $W_0$ in the mesoscopic and macroscopic levels

Therefore, $(\partial g/\partial x)_{0l}$ and $(\partial g/\partial x)_{0r}$ can be evaluated as follows:

$$\left(\frac{\partial g}{\partial x}\right)_{0l} = \overline{k}_l g_0 = (\overline{k}_{l1} + \overline{k}_{l2} c_x) g_0,$$
$$\left(\frac{\partial g}{\partial x}\right)_{0r} = \overline{k}_r g_0 = (\overline{k}_{r1} + \overline{k}_{r2} c_x) g_0 \tag{39}$$

where

$$\overline{k}_{l1} = \frac{1}{\rho}\left(\frac{\partial \rho}{\partial x}\right)_{0l} - 2\lambda u \left(\frac{\partial(\rho u)}{\partial x}\right)_{0l} + 2\lambda u^2 \left(\frac{\partial \rho}{\partial x}\right)_{0l},$$
$$\overline{k}_{l2} = -2\lambda \left(\frac{\partial(\rho u)}{\partial x}\right)_{0l} + 2\lambda u \left(\frac{\partial \rho}{\partial x}\right)_{0l} \tag{40}$$

$$\overline{k}_{r1} = \frac{1}{\rho}\left(\frac{\partial \rho}{\partial x}\right)_{0r} - 2\lambda u \left(\frac{\partial(\rho u)}{\partial x}\right)_{0r} + 2\lambda u^2 \left(\frac{\partial \rho}{\partial x}\right)_{0r},$$
$$\overline{k}_{r2} = -2\lambda \left(\frac{\partial(\rho u)}{\partial x}\right)_{0r} + 2\lambda u \left(\frac{\partial \rho}{\partial x}\right)_{0r} \tag{41}$$

$\overline{k}_r$ and $\overline{k}_l$, the slopes, shown in Fig. 3 are calculated from Eqs (37)–(39). Substituting Eq. (39) in Eq. (34), then, gives:

$$g = \begin{cases} g_0\left(1 + \overline{k}_l (x - x_{i-1/2}) + Kt\right) & x \le x_{i-1/2} \quad c_x \ge 0 \\ g_0\left(1 + \overline{k}_r (x - x_{i-1/2}) + Kt\right) & x \ge x_{i-1/2} \quad c_x < 0 \end{cases} \tag{42}$$

Up to this point, the initial velocity-distribution function $f_0$ (Eq. (33)) and the corresponding equilibrium state $g$ (Eq. (42)) at the interface $x = x_{i-1/2}$ at time $t$ have been evaluated throughout two reconstruction stages (see Fig. 3) from which the final velocity-distribution function $f$ at the interface $x = x_{i-1/2}$ and at time $t$ can be expressed:

$$\begin{aligned} &f\,(x_{i-1/2}, t, c_x) \\ &= \alpha_0\left[(1 - c_x t k_l) H(c_x) g_l + (1 - c_x t k_r)(1 - H(c_x)) g_r\right] + \alpha_1 g_0 \\ &\quad + \alpha_2\left[c_x \overline{k}_l H(c_x) g_0 + c_x \overline{k}_r (1 - H(c_x)) g_0\right] + \alpha_3 K g_0 \end{aligned} \tag{43}$$

where

$$\alpha_0 = e^{-t/\tau}, \quad \alpha_1 = 1 - e^{-t/\tau}, \quad \alpha_2 = \tau(-1 + e^{-t/\tau}) + te^{-t/\tau},$$
$$\alpha_3 = t - \tau + \tau e^{-t/\tau} \tag{44}$$

$H(c_x)$ in Eq. (43) is the Heaviside function. To evaluate $K$ in Eq. (43), the compatibility constraints are applied on the interface $x = x_{i-1/2}$ and then the result is integrated over time step $\Delta t$ as follows:

$$\int_0^{\Delta t} \int_{-\infty}^{+\infty} \left(g(x_{i-1/2}, t, c_x) - f\,(x_{i-1/2}, t, c_x)\right) \begin{bmatrix} 1 \\ c_x \end{bmatrix} \mathrm{d}c_x\, \mathrm{d}t = 0 \tag{45}$$

$g(x_{i-1/2}, t, c_x)$ evaluated from Eq. (34) at the point ($x = x_{i-1/2}$, $t$) is:

$$g(x_{i-1/2}, t, c_x) = g_0 + K g_0 t \tag{46}$$

Substituting Eqs (43) and (46) into Eq. (45) and exchanging the order of integration leads to:

$$\int_{-\infty}^{+\infty} \int_0^{\Delta t} [\alpha_0\left[H(c_x) g_l + (1 - H(c_x)) g_r\right]$$
$$- \alpha_0 t\left[c_x k_l H(c_x) g_l + c_x k_r (1 - H(c_x)) g_r\right] + (\alpha_1 - 1) g_0$$

$$+\alpha_2\big[c_x\bar{k}_l H(c_x)g_0 + c_x\bar{k}_r(1-H(c_x))g_0\big] + (\alpha_3 - t)Kg_0\Big]\begin{bmatrix}1\\ c_x\end{bmatrix}\mathrm{d}t\,\mathrm{d}c_x = 0 \tag{47}$$

Similar to the variation of $g$ with respect to $x$ (Eq. (31)), the variation of $g_0$ with respect to $t$ ($\partial g_0/\partial t = Kg_0$) yields:

$$\frac{\partial g_0}{\partial t} = Kg_0 = (K_1 + K_2 c_x)g_0 \tag{48}$$

where

$$K_1 = \frac{1}{\rho_0}\frac{\partial \rho_0}{\partial t} - 2\lambda u_0\frac{\partial(\rho_0 u_0)}{\partial t} + 2\lambda u_0^2\frac{\partial \rho_0}{\partial t} \quad \text{and}$$
$$K_2 = -2\lambda\frac{\partial(\rho_0 u_0)}{\partial t} + 2\lambda u_0\frac{\partial \rho_0}{\partial t} \tag{49}$$

The zero and first moments of Eq. (48) give:

$$\begin{bmatrix}\frac{\partial \rho_0}{\partial t}\\ \frac{\partial(\rho_0 u_0)}{\partial t}\end{bmatrix} = \int_{-\infty}^{+\infty} Kg_0\begin{bmatrix}1\\ c_x\end{bmatrix}\mathrm{d}c_x \tag{50}$$

Invoking Eq. (50), Eq. (47) finally becomes:

$$\begin{bmatrix}\frac{\partial \rho_0}{\partial t}\\ \frac{\partial(\rho_0 u_0)}{\partial t}\end{bmatrix} = \frac{1}{\beta_4}\int_{-\infty}^{+\infty}\Big[-\beta_0\big[H(c_x)g_l + (1-H(c_x))g_r\big] + \beta_1\big[c_x k_l H(c_x)g_1 + c_x k_r(1-H(c_x))g_r\big] - \beta_2 g_0 - \beta_3\big[c_x\bar{k}_l H(c_x)g_0 + c_x\bar{k}_r(1-H(c_x))g_0\big]\Big] \times \begin{bmatrix}1\\ c_x\end{bmatrix}\mathrm{d}c_x \tag{51}$$

where

$$\beta_0 = -\tau e^{-\Delta t/\tau} + \tau, \quad \beta_1 = \tau\Delta t e^{-\Delta t/\tau} + \tau^2(1 - e^{-\Delta t/\tau}),$$
$$\beta_2 = \Delta t - \tau(1 - e^{-\Delta t/\tau})$$
$$\beta_3 = -\tau\Delta t - \tau\Delta t e^{-\Delta t/\tau} + 2\tau^2(1 - e^{-\Delta t/\tau}),$$
$$\beta_4 = \tau(\Delta t + \tau(1 - e^{-\Delta t/\tau}) \tag{52}$$

where all the above coefficients are local constant. From Eq. (51), $f\,(x_{i-1/2}, t, c_x)$ can be precisely evaluated at the interface $x = x_{i-1/2}$. Therefore, the time-variant numerical fluxes at the interface $x = x_{i-1/2}$ by implementation of the moments of $g$ given in the Appendix is:

$$\boldsymbol{F}_{i-1/2} = \int_{-\infty}^{+\infty}\int_0^{\Delta t} c_x f\,(x_{i-1/2}, t, c_x)\begin{bmatrix}1\\ c_x\end{bmatrix}\mathrm{d}t\,\mathrm{d}c_x$$
$$= \gamma_0\left[\rho_l\begin{bmatrix}\langle c_x^0\rangle_{<0}\\ \langle c_x^1\rangle_{<0}\end{bmatrix} + \rho_r\begin{bmatrix}\langle c_x^0\rangle_{>0}\\ \langle c_x^1\rangle_{>0}\end{bmatrix}\right]$$
$$-\gamma_1\left[\rho_l k_{l1}\begin{bmatrix}\langle c_x^1\rangle_{<0}\\ \langle c_x^2\rangle_{<0}\end{bmatrix} + \rho_r k_{r1}\begin{bmatrix}\langle c_x^1\rangle_{>0}\\ \langle c_x^2\rangle_{>0}\end{bmatrix}\right]$$
$$-\gamma_1\left[\rho_l k_{l2}\begin{bmatrix}\langle c_x^2\rangle_{<0}\\ \langle c_x^3\rangle_{<0}\end{bmatrix} + \rho_r k_{r2}\begin{bmatrix}\langle c_x^2\rangle_{>0}\\ \langle c_x^3\rangle_{>0}\end{bmatrix}\right]$$
$$+\gamma_2\left[\rho_0\begin{bmatrix}\langle c_x^2\rangle\\ \langle c_x^3\rangle\end{bmatrix}\right] + \gamma_3\left[\rho_0\bar{k}_{l1}\begin{bmatrix}\langle c_x^1\rangle_{<0}\\ \langle c_x^2\rangle_{<0}\end{bmatrix} + \rho_0\bar{k}_{r1}\begin{bmatrix}\langle c_x^1\rangle_{>0}\\ \langle c_x^2\rangle_{>0}\end{bmatrix}\right]$$
$$+\gamma_3\left[\rho_0\bar{k}_{l2}\begin{bmatrix}\langle c_x^2\rangle_{<0}\\ \langle c_x^3\rangle_{<0}\end{bmatrix} + \rho_0\bar{k}_{r2}\begin{bmatrix}\langle c_x^2\rangle_{>0}\\ \langle c_x^3\rangle_{>0}\end{bmatrix}\right]$$
$$+\gamma_4\left[\rho_0 K_1\begin{bmatrix}\langle c_x^0\rangle\\ \langle c_x^1\rangle\end{bmatrix} + \rho_0 K_2\begin{bmatrix}\langle c_x^1\rangle\\ \langle c_x^2\rangle\end{bmatrix}\right] \tag{53}$$

where

$$\gamma_0 = \tau(1 - e^{-\Delta t/\tau}), \quad \gamma_1 = -\Delta t\tau e^{-\Delta t/\tau} - \tau^2(1 - e^{-\Delta t/\tau}),$$
$$\gamma_2 = \Delta t - \tau(1 - e^{-\Delta t/\tau})$$
$$\gamma_3 = \Delta t\tau(1 - e^{-\Delta t/\tau}), \quad \gamma_4 = \frac{1}{2}\Delta t^2 - \tau\big(\Delta t - \tau(1 - e^{-\Delta t/\tau})\big) \tag{54}$$

Similarly, time-dependent fluxes at each interface can be evaluated.

## 3 Numerical results validation and discussion

The objective of this section is to investigate the accuracy and efficiency of the proposed schemes. The test rig consists of a reservoir-pipe-valve system and a transient is generated by an instantaneous closure of the valve. For comparison, the analytical solution, Godunov-type solution (Zhao & Ghidaoui, 2004) and fixed-grid MOC with linear space-line interpolation solution (Ghidaoui & Karney, 1994; Ghidaoui, Karney, & McInnis, 1998) are used. The numerical dissipation is quantitatively measured using (i) the integrated energy method denoted by $\xi_E$ (Karney, 1990), and (ii) the $L^2$-norm method denoted by $\xi_{L^2}$ (Chaudhry & Hussaini, 1985; Ghidaoui et al., 2005). Physical friction is set to zero so as not to mask the numerical dissipation. For objective comparison between the different schemes, CPU time needed by each scheme to achieve a predetermined level of accuracy, denoted by $t_c$, is measured, all codes are run on a personal computer with a quad CPU 2.66 HZ and 4 GB memory, and all the schemes are coded by the lead author in Fortran language and compiled by the Compaq Visual Fortran compiler. It is worth mentioning that the Compaq Visual Fortran is not compatible with multi-core processors, so only a single CPU unit is involved during the computation.

Below, the accuracy and efficiency of the KFVS and BGK schemes are investigated for the test case. Note that all fluxes at the reservoir and valve interfaces are approximated using a 1st-order technique.

### 3.1 Classical water hammer test case: a sudden closure of a downstream valve

Figure 4 shows a classical reservoir-pipe-valve test case, which consists of a single frictionless pipe connected to an upstream reservoir and a downstream valve. The test case is designed to examine the ability of the mesoscopic-based schemes to capture discontinuous wave fronts induced by a sudden valve closure. This is important because a scheme that captures discontinuities means that it can handle high frequencies well.

The relevant geometric and hydraulic parameters for this test case are given in Table 1 where the initial conditions are:

$$\rho(x,t) = 1000\,\mathrm{kgm^{-3}}, \quad U(x,t) = 0.9\,\mathrm{ms^{-1}} \quad \text{for } x \in [0,L],\; t=0 \tag{55}$$

The valve and reservoir conditions are imposed at the downstream ($x = L$) and upstream ($x = 0$) of the pipe, respectively.

*KFVS scheme*

The pressure head traces at the valve produced by the 2nd-order KFVS scheme for $C_r = 0.4$ are shown in Fig. 5. The 2nd-order KFVS scheme is oscillatory for Courant numbers larger than 0.4.

The pressure traces for the 2nd-order KFVS scheme are shown in Fig. 5 with respect to $N_x$, which is the number of discretized cells in the pipe. As shown in Fig. 5, when $N_x$ increases, the pressure traces approach to the analytical solution. In addition, $E/E_0$ for different schemes is given in Fig. 6, where $E$ is the total energy (i.e. the sum of kinetic and internal energy) in the pipe proposed by Karney (1990). In the pipe, the velocity and, thus, the work at the valve are zero. In addition, the pressure wave and, thus, the work at the reservoir are zero. Moreover, the friction and, thus, the energy dissipation are zero. As result, the total energy is invariant with time: $E/E_0 = 1$, where $E_0$ is the total energy before any disturbance. Thus, any deviation of $E/E_0$ from 1 is due to numerical dissipations. $\xi_E$, shown in Fig. 6, indicates the errors calculated from the integral energy equation as follows:

$$\xi_E = 1 - \frac{E}{E_0} \tag{56}$$

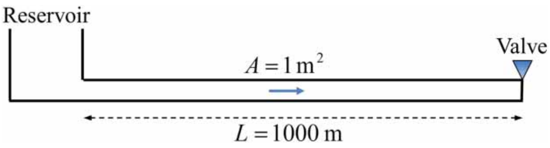

Figure 4 The system configuration for the classical water hammer test case

Table 1 The classical water hammer test case[a]

| Pipe no. | $L$ (m) | $a$ (m s$^{-1}$) | $A$ (m$^2$) |
|---|---|---|---|
| Pipe 1 | 1000 | 1000 | 1 |

[a] The discontinuous wave is evoked by a sudden valve closure of the downstream valve.

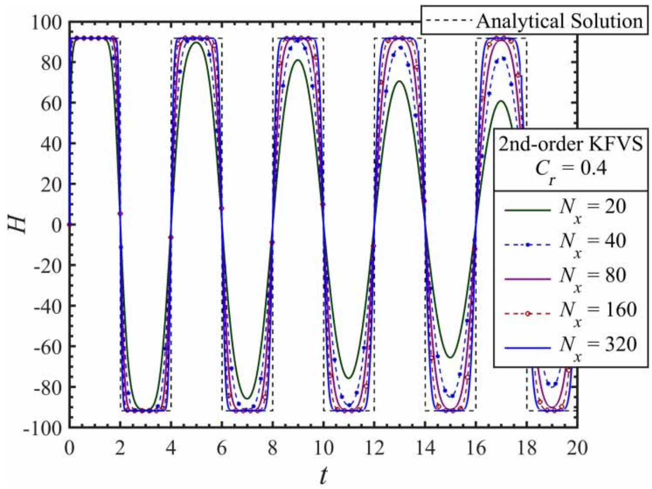

Figure 5 Pressure head traces at the valve produced by 2nd-order KFVS

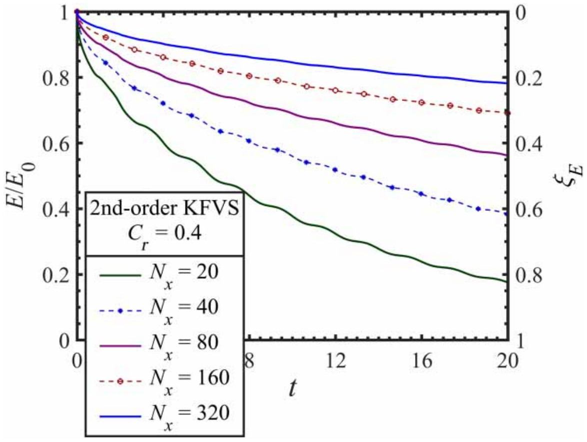

Figure 6 Energy traces for 2nd-order KFVS

*BGK scheme*

Figure 7 presents the pressure head traces at the valve produced by the BGK scheme when $C_r = 0.4$. Even though the numerical results generated by the BGK scheme converge to the analytical solution, a slight discrepancy in the form of overshoot at the discontinuity (see the magnified region in Fig. 7) is observed immediately after the valve closure and vanishes a few time steps later. The nature of the slight overshoot is found to be grid-independent and unaffected by the Courant number. Such overshoots occur despite the fact that the Van Leer limiter is used and the collision time is evaluated according to the form proposed by Xu (1998). To be specific, the collision time $\tau$

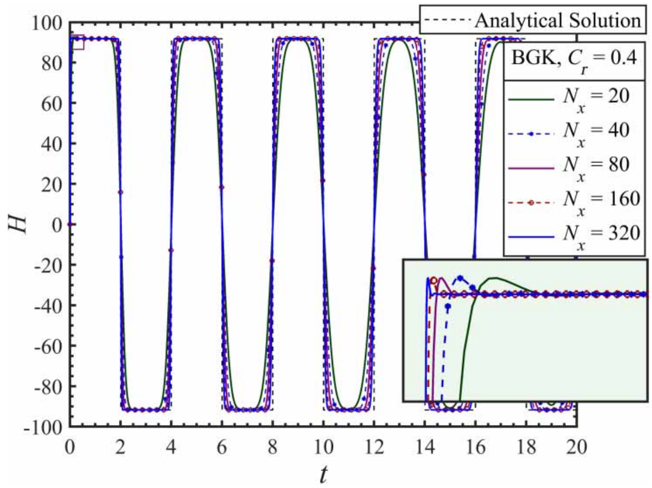

Figure 7 Pressure head traces at the valve produced by BGK

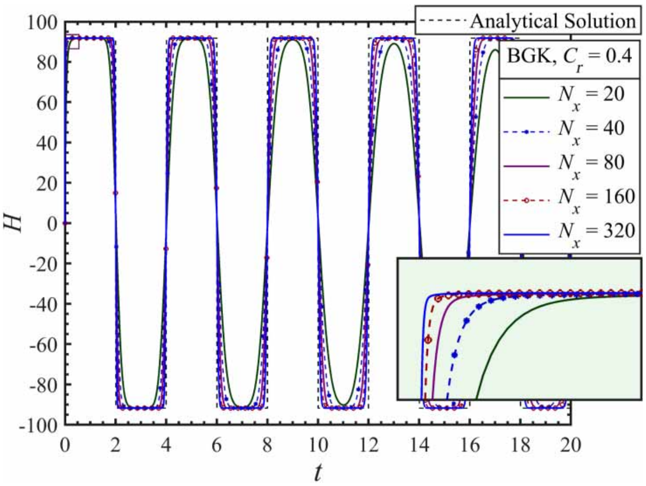

Figure 8 Pressure head traces at the valve produced by BGK with the modified collision term

adopted from Xu (1998) at the interface $x = x_{i-1/2}$ is:

$$\tau_{i-1/2} = C_1 \frac{\mu_{i-1/2}}{p_{i-1/2}} + C_2 \frac{|p_{i-1} - p_i|}{|p_{i-1} + p_i|} \Delta t \tag{57}$$

where $C_1$ and $C_2$ are constants and determined from numerical experiments. Various tests failed to cure the numerical oscillations. Therefore, further investigation is required to obtain a robust BGK scheme. The valve boundary condition (Eq. (15)) implies that $P_{N_x} = P_{N_x+1}$ and, thus, the second term in Eq. (57) is zero regardless of the value of $C_2$. To cure this problem, a modified expression for the collision time that takes into account velocity and pressure discontinuities is proposed and its form is:

$$\tau_{i-1/2} = C_1 \frac{\mu_{i-1/2}}{p_{i-1/2}} + C_2 \frac{|\rho_{i-1} U_{i-1}| - |\rho_i U_i|}{|\rho_{i-1} U_{i-1}| + |\rho_i U_i|} \Delta t \tag{58}$$

In Eq. (58), the numerical part (i.e. the second term) is more physical and is non-zero whenever there is a wave, since a wave is result of a change in flow rate. The values of $C_1$ and $C_2$ and determined by carrying out a range of numerical test cases. It is found that $C_1 = 1.0$ and $C_2 = 1.0$ produce oscillation-free results for Courant numbers equal or less than 0.5 (Fig. 8). In addition, it is found that the magnitude of $C_2$ plays a significant role in preventing the formation of artificial oscillations. For example, when $C_2 < 0.5$, the collision time is not large enough to resolve the overshoot at the discontinuity. Figure 8 shows the pressure head traces at the valve produced by the BGK scheme when $C_r = 0.4$, $C_1 = 1.0$ and $C_2 = 1.0$. The pressure traces and energy norm plots are given in Figs 8 and 9, respectively. It is found that the BGK scheme is sensitive to the Courant number and its accuracy improves as the Courant number increases to 0.5.

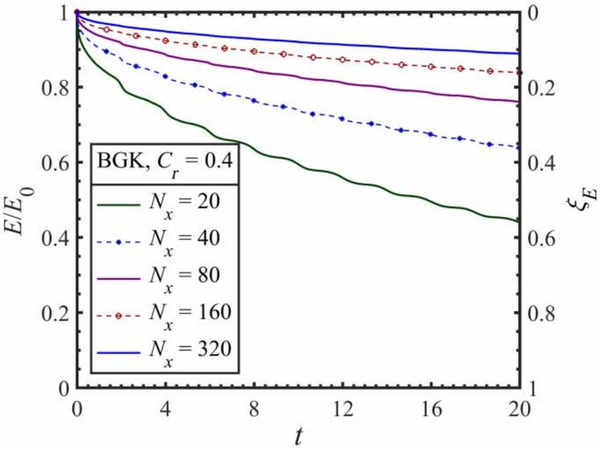

Figure 9 Energy traces for BGK with the modified collision term

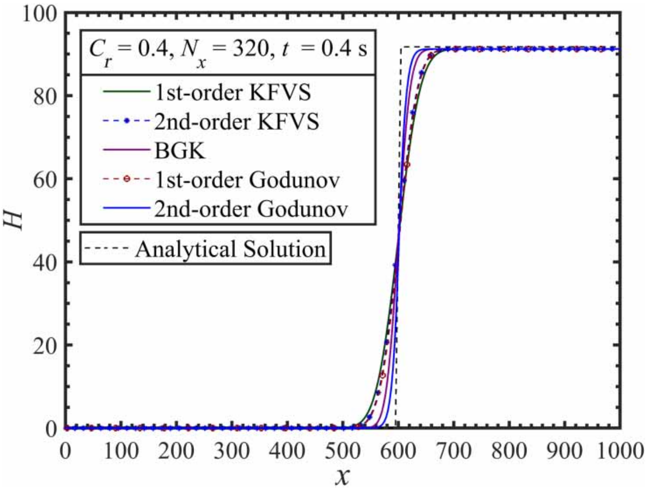

Figure 10 Discontinuous wave fronts at $t = 0.4$ s

### *Comparison between the mesoscopic-based schemes and the conventional macroscopic-based schemes*

Figure 10 compares the discontinuous wave fronts produced by the different schemes at $t = 0.4$ s. Figure 11 shows the relationship between numerical dissipation and the number of grid points at $t = 0.4$ s. $\xi_E$ for the 1st-order KFVS scheme, the 2nd-order KFVS scheme, and the BGK scheme at $N_x = 320$ are 3.58%, 3.12%, and 1.94%, respectively. In addition, both the 2nd-order KFVS scheme and the 1st-order Godunov scheme

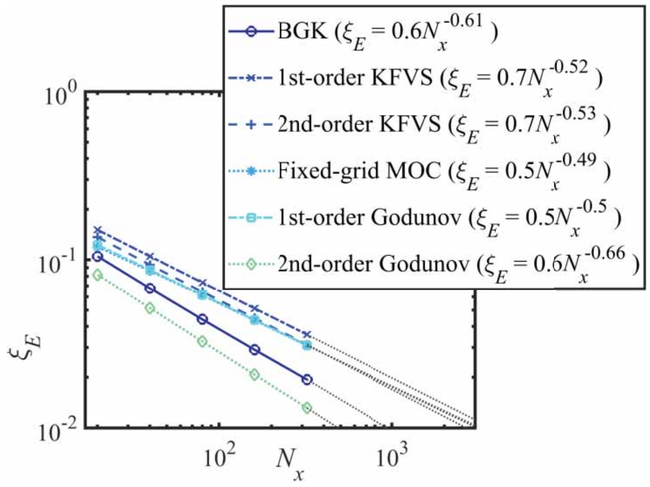

Figure 11 $\xi_E$ vs. the number of grids at $t = 0.4$ s

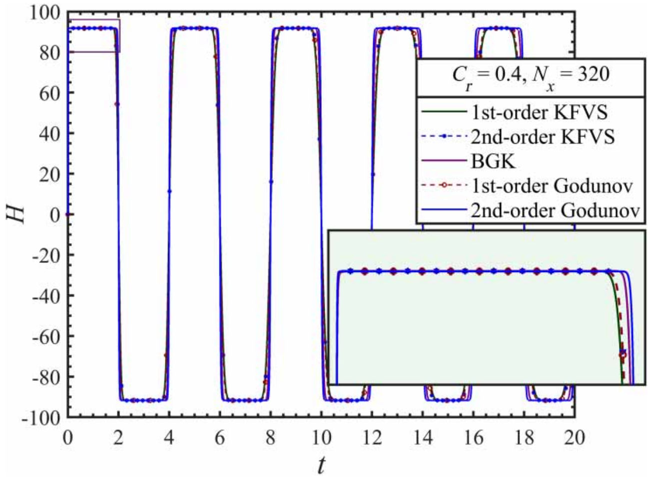

Figure 12 Comparison of pressure head traces for $N_x = 320$

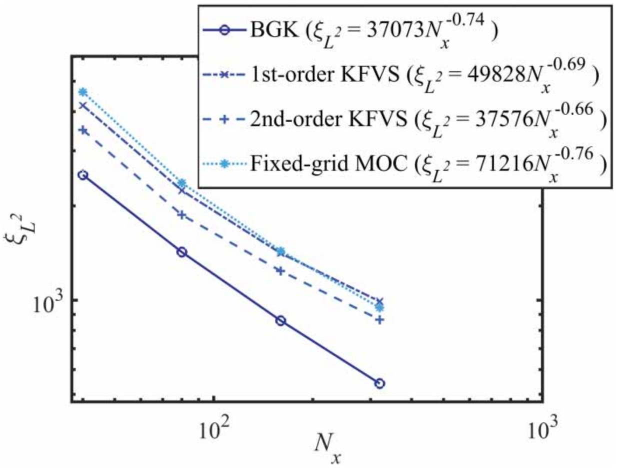

Figure 13 Comparison of $\xi_{L^2}$

produce similar results for the same grid number. The agreement between these two schemes can be quantitatively explained by the consistency of the errors shown in Fig. 13. Particularly, when $t = 0.4$ s and $N_x = 320$, $\xi_E$ for both schemes is $3.10 \pm 0.015\%$. The similarity between the 2nd-order KFVS scheme and the 1st-order Godunov scheme was also discussed by Xu (1998). It is found that the KFVS scheme is more dissipative and causes more smearing near the wave front than the other schemes. The diffusivity in the KFVS is largely due to the absence of the collision term in this model (Xu, 1998).

Figure 12 compares pressure heads produced by the different schemes for $N_x = 320$. The numerical errors measured using the $L^2$-norm method as a function of grid points is shown in Fig. 13. These results reveal that the 2nd-order Godunov scheme performed best in capturing the transient wave followed by the BGK scheme and then the KFVS schemes.

Figure 14 shows the numerical dissipation versus grid numbers and Fig. 15 shows the relation between the computational time taken by each scheme to reach the solution ($t_c$) and the number of grid points. Using these figures the CPU time needed by each scheme to achieve a predefined degree of accuracy can be estimated. For example, for $\xi_E = 20\%$, the number of grids required by the 1st-order KFVS scheme, 2nd-order KFVS scheme, BGK scheme, 1st-order Godunov scheme, 2nd-order Godunov scheme and fixed-grid MOC is roughly evaluated 550,

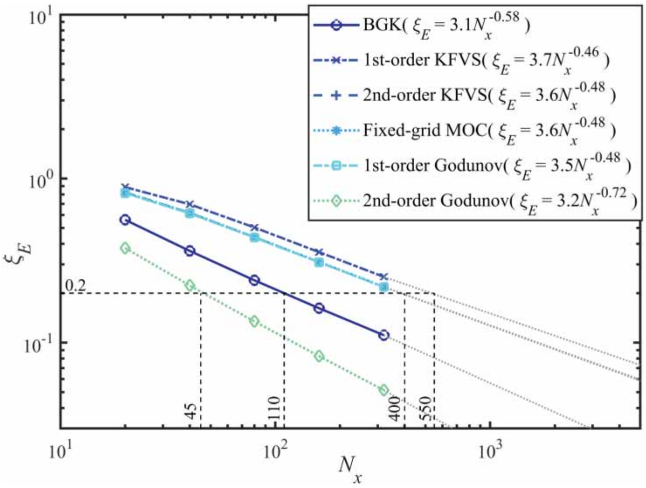

Figure 14 Relation between $\xi_E$ and the number of grids

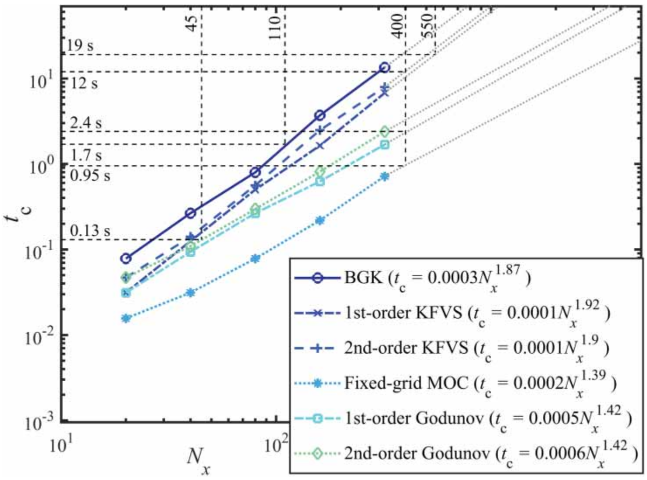

Figure 15 Relation between the computational time and the number of grids

400, 110, 400, 45 and 400, respectively (Fig. 14). Consequently, the computational times taken by the 1st-order KFVS scheme, 2nd-order KFVS scheme, BGK scheme, 1st-order Godunov scheme, 2nd-order Godunov scheme and fixed-grid MOC to achieve $\xi_E = 20\%$ are approximated 19 , 12 , 1.7 , 2.4 , 0.13 and 0.95 s, respectively (Fig. 15). Note that errors associated with all schemes represented in Figs 14 and 15 are grid-dependent and $C_r$-dependent. However, the results are produced for $C_r = 0.4$, which is the maximum Courant number for which all schemes are stable. It is noted that fixed-grid MOC for $C_r = 0.4$ are extremely dissipative; in practice, the performance of fixed-grid MOC can be drastically improved by halving the grid size ($C_r = 0.8$).

The convergence rate of the 2nd-order KFVS is slightly larger than that of the 1st-order KFVS scheme. The BGK scheme, however, converges 6–10 times faster than the KFVS schemes. The 2nd-order Godunov scheme has the best convergence rate of all schemes tested.

## 4 Conclusion

This study is motivated by the need for a high resolution scheme for water hammer waves when these waves are being used as a tool for pipe condition assessment. Boltzmann (mesoscopic) based schemes (KFVS and BGK schemes) are formulated and are compared to Godunov-type schemes as well as fixed-grid MOC. The key results are as follows:

- Two mesoscopic approaches (BGK and KFVS) are successfully formulated and applied to a simple pipeline system.
- Comparison between the efficiency of fixed-grid MOC scheme, Godunov scheme, KFVS scheme and BGK scheme reveals that the 2nd-order Godunov scheme is the best followed closely by the BGK scheme.
- The absence of collision in the KFVS scheme means that this scheme is more dissipative than the BGK scheme. However, the KFVS scheme is far easier to derive and code than the BGK scheme.
- The BGK, KFVS and Godunov schemes are all FV schemes; thus, mass and momentum conservation are guaranteed by these techniques.
- It is found that the numerical part of the collision time in the BGK scheme needs to be modified in order to produce an oscillation-free solution. The proposed modification is based on the fact that water hammer waves are generally associated with a change in flow. Therefore, making the numerical part of the collision a function of a change in flow guarantees that this part is non-zero whenever there is a wave.
- The stability of the proposed FV schemes is satisfied when $C_r < 0.5$. The restriction on $C_r$ is mainly due to the kinetic approach where not only the mean velocity plays a role in the stability condition, but also particle's velocities, ranging from $-\infty$ to $+\infty$, contribute to the stability.

The development of one-dimensional FV methods for water hammer flows is the prerequisite for the progress of high frequency wave theory in pipes. Indeed, Louati and Ghidaoui (2017), the research group of the second author, successfully implemented the Godunov and Boltzmann type schemes for multi-dimensional water hammer flows using directional splitting. Their results are highly promising and their multi-dimensional models serve as a tools to study properties of three-dimensional water hammer waves inside pipes.

## Funding

The research is financially supported by the Research Grant Council (RGC), Hong Kong [grants 612511, 612713 and T21-602/15R].

## Appendix. Specification of the Gaussian velocity-distribution function for water hammer problems and its moments

In this section a Gaussian velocity-distribution function is specified for water hammer problems using H-theorem. Based on the H-theorem, entropy (Eq. (2)) monotonically increases with time, and attains its maximum value at an equilibrium state. The maximum entropy can be obtained subject to Eq. (7) (i.e. the constraints) using the Lagrange multipliers method. An arithmetic combination of Eq. (7), multiplied by $\sigma_0$, $\sigma_1$, and $\sigma_2$, respectively (i.e. the Lagrange multipliers), and Eq. (2) in the one-dimensional form gives:

$$S = -\int_{-\infty}^{+\infty} \left[ f\ \ln(f) + \sigma_0 f + \sigma_1 c_x f + \sigma_2 c_x^2 f \right] \mathrm{d}c_x + \sigma_0 \rho + \sigma_1 \rho u + \sigma_2 \rho \left( u^2 + \frac{P}{\rho} \right) \tag{A1}$$

where $P = \rho a^2$ (Eq. (12)). The Lagrange multipliers can be obtained by analysing a total deviation of $S$ in Eq. (A1) with respect to $f$, $\rho$ and $u$ for fixed $t$, $x$, and $c_x$ around the equilibrium state while the Lagrange multipliers are held constant. $f$, $\rho$ and $u$ are independent variables, consequently their variations are independent, so the deviation of the entropy can be written:

$$\delta S = -\int_{-\infty}^{+\infty} \delta f \left[ \ln(f) + 1 + \sigma_0 + \sigma_1 c_x + \sigma_2 c_x^2 \right] \mathrm{d}c_x + \delta\rho\left[\sigma_0 + \sigma_1 u + \sigma_2 (u^2 + a^2)\right] + \delta u\left[\sigma_1 \rho + 2\sigma_2 u \rho\right] \tag{A2}$$

In the maximum entropy, variation of entropy at the equilibrium state is zero ($\delta S = 0$). Therefore, the coefficients of the independent variations ($\delta f$ , $\delta\rho$ and $\delta u$) in Eq. (A2) should be zero:

$$\ln(f) + 1 + \sigma_0 + \sigma_1 c_x + \sigma_2 c_x^2 = 0 \tag{A3}$$

$$\sigma_0 + \sigma_1 u + \sigma_2 (u^2 + a^2) = 0 \tag{A4}$$

$$\sigma_1 \rho + 2\sigma_2 u \rho = 0 \tag{A5}$$

Eq. (A3) can be rewritten:

$$f = e^{-1-\sigma_0} e^{-\sigma_1 c_x - \sigma_2 c_x^2} \tag{A6}$$

where $f$ is the one-dimensional Gaussian-typed function. Substituting Eq. (A6) into Eq. (7) and integrating with respect to particle velocities (i.e. $c_x$) gives:

$$\rho = \int_{-\infty}^{+\infty} (e^{-1-\sigma_0} e^{-\sigma_1 c_x - \sigma_2 c_x^2})\, \mathrm{d}c_x = e^{-1-\sigma_0} \left(\frac{\pi}{\sigma_2}\right)^{1/2} e^{(\sigma_1^2/4\sigma_2)} \tag{A7}$$

$$\begin{aligned} \rho u &= \int_{-\infty}^{+\infty} (c_x e^{-1-\sigma_0} e^{-\sigma_1 c_x - \sigma_2 c_x^2})\, \mathrm{d}c_x \\ &= e^{-1-\sigma_0} \frac{\sigma_1}{2\sigma_2} \left(\frac{\pi}{\sigma_2}\right)^{1/2} e^{(\sigma_1^2/4\sigma_2)} \end{aligned} \tag{A8}$$

$$\begin{aligned} \rho(u^2 + a^2) &= \int_{-\infty}^{+\infty} (c_x c_x e^{-1-\sigma_0} e^{-\sigma_1 c_x - \sigma_2 c_x^2})\, \mathrm{d}c_x \\ &= e^{-1-\sigma_0} \frac{1}{2\sigma_2} \left(1 + \frac{\sigma_1^2}{2\sigma_2}\right) \left(\frac{\pi}{\sigma_2}\right)^{1/2} e^{(\sigma_1^2/4\sigma_2)} \end{aligned} \tag{A9}$$

A combination of Eqs (A7) and (A9) gives the Lagrange multiplier coefficients as follows:

$$\sigma_1 = -\frac{\rho u}{P}, \qquad \sigma_2 = -\frac{\rho}{2P} \tag{A10}$$

The insertion of $\sigma_1$ and $\sigma_2$ into Eq. (A6) leads to:

$$e^{-1-\sigma_0} = \rho \left(1/\left(\frac{2\pi P}{\rho}\right)\right)^{1/2} e^{-\rho u^2/2P} \tag{A11}$$

Substituting $\sigma_1$ and $\sigma_2$ and Eq. (A11) into Eq. (A6) gives the velocity-distribution function for one-dimensional problems below:

$$f = \rho \sqrt{\frac{1}{2\pi a^2}} e^{\left(-(c_x - u)^2/2a^2\right)} \tag{A12}$$

In maximum entropy, $f$ approaches $g$ and the mean and the standard deviation of $g$ (i.e. Maxwellian velocity-distribution function) are $u$ and $a^2$, respectively.

The moments of the one-dimensional Gaussian velocity-distribution function specified for water hammer problem depend on the integration limits are given in the coming part. For simplicity, let us introduce the moments of $g$ by the following notation:

$$\rho \left\langle c_x^m \right\rangle = \int_{-\infty}^{+\infty} c_x^m g \, \mathrm{d}c_x, \tag{A13}$$

where $m$ is an integer. The values of $\rho\langle c_x^m\rangle$, in different $m$, for different integration limits represent below.

(1) $\rho\langle c_x^m\rangle$ for $-\infty < c_x < +\infty$

$$\begin{pmatrix} \left\langle c_x^0 \right\rangle \\ \left\langle c_x^1 \right\rangle \\ \vdots \\ \left\langle c_x^n \right\rangle \end{pmatrix} = \begin{pmatrix} 1 \\ u \\ \vdots \\ u \left\langle c_x^{n-1} \right\rangle + \frac{n-1}{2\lambda} \left\langle c_x^{n-2} \right\rangle \end{pmatrix} \tag{A14}$$

(2) $\rho\langle c_x^m\rangle$ for $0 < c_x < +\infty$:

$$\begin{pmatrix} \left\langle c_x^0 \right\rangle_{>0} \\ \left\langle c_x^1 \right\rangle_{>0} \\ \vdots \\ \left\langle c_x^n \right\rangle_{>0} \end{pmatrix} = \begin{pmatrix} \frac{1}{2} \mathrm{erfc}(-\sqrt{\lambda} u) \\ u \left\langle c_x^0 \right\rangle_{>0} + \frac{1}{2} \frac{e^{-\lambda u^2}}{\sqrt{\pi \lambda}} \\ \vdots \\ u \left\langle c_x^{n-1} \right\rangle_{>0} + \frac{n-1}{2\lambda} \left\langle c_x^{n-2} \right\rangle_{>0} \end{pmatrix} \tag{A15}$$

(3) $\rho\langle c_x^m\rangle$ for $-\infty < c_x < 0$:

$$\begin{pmatrix} \left\langle c_x^0 \right\rangle_{<0} \\ \left\langle c_x^1 \right\rangle_{<0} \\ \vdots \\ \left\langle c_x^n \right\rangle_{<0} \end{pmatrix} = \begin{pmatrix} \frac{1}{2} \mathrm{erfc}(\sqrt{\lambda} u) \\ u \left\langle c_x^0 \right\rangle_{<0} - \frac{1}{2} \frac{e^{-\lambda u^2}}{\sqrt{\pi \lambda}} \\ \vdots \\ u \left\langle c_x^{n-1} \right\rangle_{<0} + \frac{n-1}{2\lambda} \left\langle c_x^{n-2} \right\rangle_{<0} \end{pmatrix} \tag{A16}$$

The complementary error function appears in the formulation when the moments are considered for the positive or negative half space.

## Notation

$A$ = pipe cross-sectional area (m$^2$)
$a$ = transient wave speed (m s$^{-1}$)
$\boldsymbol{C}$ = particle velocities (m s$^{-1}$)
$C_1$ = coefficient of collision time (–)
$C_2$ = coefficient of collision time (–)
$C_r$ = Courant number (–)
$c_x$ = particle velocities in $x$-direction (m s$^{-1}$)
$c_y$ = particle velocities in $y$-direction (m s$^{-1}$)
$c_z$ = particle velocities in $z$-direction (m s$^{-1}$)
$D$ = pipe diameter (mm)
$E$ = sum of total kinetic energy and total internal energy (J)
erfc(·) = complementary error function (–)
$\boldsymbol{F}$ = numerical time-dependent fluxes along $x$-direction (kg m$^{-2}$, kg m$^{-1}$s$^{-1}$)

$\boldsymbol{F}'$ = external forces (N)
$f$ = non-equilibrium velocity-distribution function (–)
$f_0$ = non-equilibrium velocity-distribution function at the beginning of each time step (–)
$g$ = equilibrium velocity-distribution function (–)
$H$ = pressure head (m)
$\mathrm{H}(\cdot)$ = Heaviside function (–)
$i$ = cell number (–)
$Kg_0$ = temporal gradient of $g_0$ ($\mathrm{s}^{-1}$)
$k$ = corresponding slope of Maxwellian function ($\mathrm{m}^{-1}$)
$L$ = length of pipe (m)
$N_x$ = the number of cells in the space domain (–)
$n$ = time index (–)
$P$ = fluid pressure (Pa)
$Q$ = flow rate ($\mathrm{m}^3\,\mathrm{s}^{-1}$)
$S$ = entropy function (–)
$t$ = time (s)
$t'$ = dummy variable (s)
$t_\mathrm{c}$ = computational time (s)
$U$ = average macroscopic flow velocity in $x$-direction ($\mathrm{m\,s}^{-1}$)
$u$ = macroscopic flow velocity in $x$-direction ($\mathrm{m\,s}^{-1}$)
$\boldsymbol{W}$ = flow variable ($\mathrm{kg\,m}^{-3}$, $\mathrm{kg\,m}^{-3}\,\mathrm{m\,s}^{-1}$)
$\boldsymbol{X}$ = position (m)
$x$ = position in $x$-direction (m)
$x'$ = trajectory of a particle motion (m)
$y$ = position in $y$-direction (m)
$z$ = position in $z$-direction (m)
$\Delta t$ = numerical time step (s)
$\Delta x$ = numerical cell (grid) size (m)
$\lambda$ = $1/2a^2$ ($\mathrm{m}^{-2}\,\mathrm{s}^2$)
$\mu$ = dynamic viscosity (Pa s)
$\xi_E$ = error calculated from the integrated energy method (–)
$\xi_{L^2}$ = error calculated from the $L^2$-norm method (m)
$\sigma$ = coefficient of Lagrange multiplier (–)
$\rho$ = density ($\mathrm{kg\,m}^{-3}$)
$\tau$ = collision time (s)
$\omega$ = frequency (Hz)
BGK = Bhatnagar-Gross-Krook
FV = finite volume
KFVS = kinetic flux vector splitting
MOC = method of characteristics

## References

Cercignani, C. (1988). The boltzmann equation. In *The Boltzmann equation and its applications* (pp. 40–103). New York, NY: Springer.

Chaudhry, M. H. (1979). *Applied hydraulic transients*. New York: Springer.

Chaudhry, M. H., & Hussaini, M. Y. (1985). Second-order accurate explicit finite-difference schemes for waterhammer analysis. *Journal of Fluids Engineering*, *107*(4), 523–529.

Cheng, Y. G., Zhang, S. H., & Chen, J. Z. (1998). Water hammer simulation by the lattice Boltzmann method. *Transactions of the Chinese Hydraulic Engineering Society, Journal of Hydraulic Engineering*, *6*, 25–31 (in Chinese).

Duan, H. F., Lee, P., & Ghidaoui, M. (2014). Transient wave-blockage interaction in pressurized water pipelines. *Procedia Engineering*, *70*, 573–582.

Duan, H. F., Lee, P. J., Che, T. C., Ghidaoui, M. S., Karney, B. W., & Kolyshkin, A. A. (2017). The influence of non-uniform blockages on transient wave behavior and blockage detection in pressurized water pipelines. *Journal of Hydro-environment Research*, *17*, 1–7.

Ghidaoui, M., Deng, J., Gray, W., & Xu, K. (2001). A Boltzmann–based model for open channel flows. *International Journal for Numerical Methods in Fluids*, *35*(4), 449–494.

Ghidaoui, M. S. (2008). What does kinetic theory have to do with hydraulics?. *Journal of Hydraulic Engineering*, *134*(7), 879–884.

Ghidaoui, M. S., & Karney, B. W. (1994). Equivalent differential equations in fixed-grid characteristics method. *Journal of Hydraulic Engineering*, *120*(10), 1159–1175.

Ghidaoui, M. S., Karney, B. W., & McInnis, D. A. (1998). Energy estimates for discretization errors in water hammer problems. *Journal of Hydraulic Engineering*, *124*(4), 384–393.

Ghidaoui, M. S., & Liang, J. H. (2008). Investigation of shallow mixing layers by BGK finite volume model. *International Journal of Computational Fluid Dynamics*, *22*(7), 523–537.

Ghidaoui, M. S., Zhao, M., McInnis, D. A., & Axworthy, D. H. (2005). A review of water hammer theory and practice. *Applied Mechanics Reviews*, *58*(1), 49–76.

Guinot, V. (2000). Riemann solvers for water hammer simulations by Godunov method. *International Journal for Numerical Methods in Engineering*, *49*(7), 851–870.

Hirsch, C. S. (2007). *Numerical computation of internal and external flows: Fundamentals of computational fluid dynamics* (2nd ed.). Amsterdam: Elsevier, ButterworthHeinemann.

Hwang, Y. H., & Chung, N. M. (2002). A fast Godunov method for the water-hammer problem. *International Journal for Numerical Methods in Fluids*, *40*(6), 799–819.

Karney, B. W. (1990). Energy relations in transient closed-conduit flow. *Journal of Hydraulic Engineering*, *116*(10), 1180–1196.

Kogan, M. N. (1967). *Dinamika razrezhennogo gaza. Kineticheskaya teoriya* [Dynamics of a Rarefied Gas: Kinetic Theory]. Moscow: Nauka.

Lee, P., Tuck, J., Davidson, M., & May, R. (2017). Piezoelectric wave generation system for condition assessment of field water pipelines. *Journal of Hydraulic Research*, *55*(5), 721–730.

Lee, P. J., Duan, H. F., Tuck, J., & Ghidaoui, M. (2014). Numerical and experimental study on the effect of signal bandwidth on pipe assessment using fluid transients. *Journal of Hydraulic Engineering*, *141*(2), 04014074.

Li, N. (2001). *A kinetic flux vector splitting scheme for open channel flows* (Master's thesis). Hong Kong University of Science and Technology, Hong Kong, China.

Li, Z., Jing, L., & Murch, R. (2017). Propagation of monopole source excited acoustic waves in a cylindrical high-density polyethylene pipeline. *The Journal of the Acoustical Society of America*, *142*(6), 3564–3579.

Liang, J. H., Ghidaoui, M. S., Deng, J. Q., & Gray, W. G. (2007). A Boltzmann-based finite volume algorithm for surface water flows on cells of arbitrary shapes. *Journal of Hydraulic Research*, *45*(2), 147–164.

Liu, H., Xu, K., Zhu, T., & Ye, W. (2012). Multiple temperature kinetic model and its applications to micro-scale gas flows. *Computers and Fluids*, *67*, 115–122.

Louati, M., & Ghidaoui, M. S. (2016, November). On the behaviour of high frequency acoustic waves in pressurized inviscid fluid in a conduit. In *12th international conference-pressure surges 2015*, Dublin, Ireland.

Louati, M., & Ghidaoui, M. S. (2017). High-frequency acoustic wave properties in a water-filled pipe. Part 1: Dispersion and multi-path behaviour. *Journal of Hydraulic Research*, *55*(5), 613–631.

Lui, S. H., & Xu, K. (2001). Entropy analysis of kinetic flux vector splitting schemes for the compressible Euler equations. *Zeitschrift für Angewandte Mathematik und Physik ZAMP*, *52*(1), 62–78.

Meniconi, S., Duan, H. F., Lee, P. J., Brunone, B., Ghidaoui, M. S., & Ferrante, M. (2013). Experimental investigation of coupled frequency and time-domain transient test-based techniques for partial blockage detection in pipelines. *Journal of Hydraulic Engineering*, *139*(10), 1033–1040.

Mesgari Sohani, S., & Ghidaoui, M. S. (2018). Formulation of consistent finite volume schemes for hydraulic transients. *Journal of Hydraulic Engineering*. doi:10.1080/00221686.2018.1522376

Toro, E. F. (2009). *Riemann solvers and numerical methods for fluid dynamics: A practical introduction* (3rd ed.). Berlin: Springer Science & Business Media.

Van Leer, B. (1997). Towards the ultimate conservative difference scheme. *Journal of Computational Physics*, *135*(2), 229–248.

Villani, C. (2008). H-Theorem and beyond: Boltzmann's entropy in today's mathematics. In *Boltzmann's legacy, ESI Lectures In Mathematics and Physics, European Mathematical Society* (pp. 129–143), Zürich.

Vincenti, W. G., & Kruger, C. H. (1965). *Introduction to physical gas dynamics* (Vol. *246*). New York: Wiley.

Xu, K. (1997). BGK-based scheme for multicomponent flow calculations. *Journal of Computational Physics*, *134*(1), 122–133.

Xu, K. (1998). Gas-kinetic schemes for unsteady compressible flow simulations. *Lecture Series-van Kareman Institute for Fluid Dynamics (VKI)*, *3*, C1–C202.

Xu, K. (1999). A gas-kinetic scheme for the Euler equations with heat transfer. *SIAM Journal on Scientific Computing*, *20*(4), 1317–1335.

Xu, K., & He, X. (2003). Lattice Boltzmann method and gas-kinetic BGK scheme in the low-mach number viscous flow simulations. *Journal of Computational Physics*, *190*(1), 100–117.

Xu, K., Kim, C., Martinelli, L., & Jameson, A. (1996). BGK-based schemes for the simulation of compressible flow. *International Journal of Computational Fluid Dynamics*, *7*(3), 213–235.

Xu, K., Mao, M., & Tang, L. (2005). A multidimensional gas-kinetic bgk scheme for hypersonic viscous flow. *Journal of Computational Physics*, *203*(2), 405–421.

Yongguang, C., Shihua, Z., & Jianzhi, C. (1998). Water hammer simulation by the lattice Boltzmann method. *Journal of Hydraulic Engineering*, *6*, 25–31.

Zhang, S. Q., Ghidaoui, M. S., Gray, W. G., & Li, N. Z. (2003). A kinetic flux vector splitting scheme for shallow water flows. *Advances in Water Resources*, *26*(6), 635–647.

Zhao, M., & Ghidaoui, M. S. (2004). Godunov-type solutions for water hammer flows. *Journal of Hydraulic Engineering*, *130*(4), 341–348.

Zhao, M., Ghidaoui, M. S., Louati, M., & Duan, H. F. (2018). Numerical study of the blockage length effect on the transient wave in pipe flows. *Journal of Hydraulic Research*, *56*(2), 245–255.